

Scanning tunneling spectroscopy of magnetic quantum impurities in two-dimensional magnets

Tim Bauer,¹ Lucas R. D. Freitas,² Eric Andrade,³ Reinhold Egger,¹ and Rodrigo G. Pereira²

¹*Institut für Theoretische Physik, Heinrich-Heine-Universität, D-40225 Düsseldorf, Germany*

²*International Institute of Physics and Departamento de Física Teórica e Experimental, Universidade Federal do Rio Grande do Norte, Natal, RN, 59078-970, Brazil*

³*Instituto de Física, Universidade de São Paulo, 05315-970 São Paulo, SP, Brazil*

We study scanning tunneling spectroscopy (STS) of magnetic quantum impurities in (partially) polarized phases of two-dimensional (2D) van der Waals magnets. Focusing on the Kitaev-Heisenberg honeycomb model for transition metal trihalides, e.g., CrI_3 or $\alpha\text{-RuCl}_3$, we consider adatom and substitutional impurity positions. Unlike the non-magnetic case, magnetic impurities can induce bound states below the magnon gap, whose energy one can measure by STS at finite bias voltage. Whenever the bound state energy vanishes as function of the magnetic field, we predict discontinuous local spin transitions which are expected to be ubiquitous in 2D magnets. They can be detected by STS in the zero-bias limit.

Introduction.—Understanding the fascinating properties of the recently discovered 2D van der Waals magnets is a topic of enormous current interest; for reviews, see [1–7]. These materials can be directly studied by surface probe techniques. In particular, their local magnetization profile has been mapped out by scanning nitrogen-vacancy magnetometry and by magnetic force microscopy [7]. With the atomic resolution offered by STS [8], one may examine single-atom spin-flip processes and spin excitations localized near impurities in full detail [9, 10]. In this Letter, we provide a theory of STS for magnetic quantum impurities in (partially) polarized phases of 2D magnets. For concreteness, we focus on the honeycomb lattice structure realized in transition metal trihalides [7]. This material class includes CrI_3 , a celebrated 2D ferromagnet with a small spin gap due to anisotropic exchange interactions [11–16]. A second example is the layered Kitaev material $\alpha\text{-RuCl}_3$ [17–20]. In the latter, the effects of dilute Cr^{3+} magnetic impurities have been linked to the Kondo screening by a Majorana metal phase [21], but magnon bound states may also potentially affect the low-energy spectrum. We note that STS observations of bound states induced by magnetic impurities in the spin-liquid candidate TaSe_2 have been interpreted as spinon-Kondo effect [22, 23]. Similar bound states have been studied in the context of the Kondo effect in spin chains [24], a problem of relevance also for nanographene chains [25, 26].

For 2D magnets in a magnetic field, non-magnetic impurities (such as vacancies or bond defects) are generally *not* expected to induce bound states below the magnon gap. For instance, for the 2D Kitaev honeycomb model [27–33] in a partially polarized phase [34–36], non-magnetic impurities generate magnon bound states only inside the energy gap between magnon bands of opposite Chern number [37, 38]. These bound states are precursors of the chiral edge states in topological magnon phases [35, 36, 39–41]. On the other hand, for a classical magnetic impurity (with spin $S_{\text{imp}} \gg 1$), which is

equivalent to a local magnetic field, bound states below the magnon gap have been predicted [38]. This effect is independent of the band topology. Noting that the local field acts as an attractive potential for a particle (the magnon) in 2D space, the bound state energy can be analytically determined, see the Supplementary Material (SM) [42].

We here include quantum fluctuations of the magnetic impurity by using exact diagonalization (ED) for small lattices and linear spin wave (LSW) theory in the thermodynamic limit. Quantum effects are shown to *qualitatively* change the scaling properties of the sub-gap bound state energy. Depending, in particular, on the values of the bulk (S) and the impurity (S_{imp}) spins and on the impurity position type (e.g., adatom vs substitutional), the bound state energy can reach zero multiple times as function of control parameters such as the magnetic field. Whenever this happens, we predict a *discontinuity* in the local magnetization of the impurity and/or its neighboring bulk spins. Such discontinuous spin transitions manifest themselves as pronounced steps in the control parameter dependence of the zero-bias STS conductance. By scanning the STS conductance at finite bias voltage, one obtains information about the bound state energy. Moreover, by performing spatial STS scans in the vicinity of the impurity, the impurity type can be fully resolved. Such bound state effects due to magnetic impurities are expected to arise in general for 2D van der Waals magnets. We showcase them here for the partially polarized phase of the Kitaev-Heisenberg honeycomb model [43] for transition metal trihalides like CrI_3 and $\alpha\text{-RuCl}_3$.

General setup.—We consider 2D spin Hamiltonians of the form ($\hbar = e = 1$ below)

$$H = \sum_{\langle j,k \rangle} \mathbf{S}_j^T H_{j,k} \mathbf{S}_k - \sum_j \mathbf{h}_j \cdot \mathbf{S}_j, \quad (1)$$

where $\mathbf{S}_j = (S_j^x, S_j^y, S_j^z)^T$ is a spin operator at site j , $\langle j, k \rangle$ denotes a bond between neighboring sites, $H_{j,k}$ are

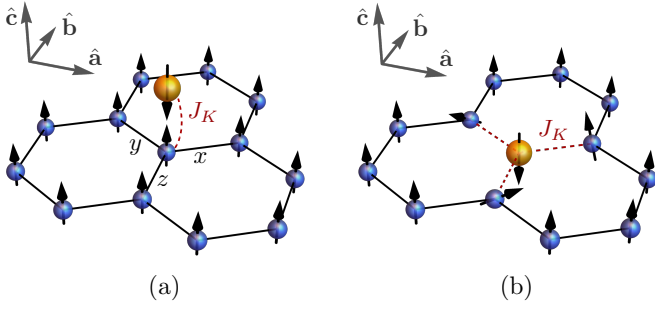


Figure 1. Sketch of a (small part of a) 2D magnet with honeycomb lattice structure (bulk spins are shown in blue) and a single magnetic quantum impurity (yellow). Coordinate unit vectors (\hat{a} , \hat{b} , \hat{c}) and nearest-neighbor bond types (x , y , z) are also indicated. (a) Adatom position of the impurity with isotropic exchange coupling $J_K > 0$ to a single bulk spin. (b) Substitutional position, where the impurity replaces one bulk spin and interacts through isotropic couplings $J_K > 0$ with the three neighboring bulk spins. Here we schematically illustrate that, in general, the classical spin configuration minimizing the energy can be inhomogeneous due to spin canting in the vicinity of the impurity [42, 44–47].

spin-spin coupling matrices, and the vector \mathbf{h}_j is proportional to the local magnetic field at site j . The bulk sites are occupied by spins S , and there is a single magnetic impurity with spin S_{imp} . We denote the impurity site by $j = 0$, which is included in the summations in Eq. (1). The bulk spins reside on a honeycomb lattice, where we consider two types of impurity locations as illustrated in Fig. 1. In the *adatom* case, the magnetic impurity couples to a single bulk spin. In the *substitutional* case, one replaces a single bulk spin by the impurity spin which then couples to the three neighboring bulk spins. For other configurations, e.g., if the impurity is located in the center of a hexagonal plaquette and thus couples to six bulk spins, results can be obtained by adapting our calculations for the cases considered here. For anisotropic exchange interactions, spin-rotational symmetry is absent, but the bulk spin coupling matrix $H_{j,k}$ can be constrained by the space group symmetry of the lattice [48]. As paradigmatic model for transition metal trihalides, we consider the Kitaev-Heisenberg honeycomb model [43] for bulk spin $S = 3/2$ and ferromagnetic bulk exchange coupling $J_b > 0$. For CrI_3 , first-principles calculations and analysis of experimental data [49–51] indicate a subdominant antiferromagnetic Kitaev coupling $K < 0$. In the SM, we also present results for the idealized ferromagnetic ($K > 0$, $J_b = 0$) Kitaev model with $S = 1/2$ [27]. We note that it is straightforward to generalize our approach to include other couplings, e.g., Dzyaloshinskii-Moriya interactions between next-nearest neighbors.

For the impurity-bulk spin couplings in Fig. 1, we instead consider an isotropic antiferromagnetic exchange coupling, $H_{0,j} = J_K \mathbb{1}_3$ with $J_K > 0$. This is a natural

assumption if the impurity atom has no orbital degeneracy [21]. Next, we recall that for a free magnetic ion with spin S , orbital angular momentum L , and total angular momentum J , the Landé factor is $g_L = \frac{3}{2} + \frac{S(S+1) - L(L+1)}{2J(J+1)}$ [52]. This value is typically a good approximation for $4f$ ions like Yb^{3+} , where crystal field effects are weak and J follows from Hund’s rules. On the other hand, for $3d$ ions like Cr^{3+} , L is quenched by crystal field effects and hence $g_L = 2$ for all S . For Ru^{3+} ions in $\alpha\text{-RuCl}_3$, the intricate interplay between orbital degeneracy, crystal field, and spin-orbit coupling [53] implies that g_L is an anisotropic tensor [52]. Reported values are $g_L^{ab} \approx 2.3$ and $g_L^c \approx 1.3$ for magnetic fields parallel and perpendicular to the ab plane, respectively [54]. Assuming a homogeneous external magnetic field, we absorb the Bohr magneton and the bulk Landé factor into $\mathbf{h}_j = \mathbf{h}$ in Eq. (1) for bulk sites ($j \neq 0$). For the impurity spin ($j = 0$), we set

$$\mathbf{h}_0 = g\mathbf{h}, \quad g = g_L^{\text{imp}}/g_L^{\text{bulk}}, \quad (2)$$

where g is the relative Landé factor of the impurity compared to the bulk spins. For instance, for Ru^{3+} ions and $\mathbf{h} = h\hat{c}$, one finds $g \approx 1.5$ and $S_{\text{imp}} = 1/2$ both for Co adatoms [22] and for Ti^{3+} ions at substitutional sites.

Before turning to concrete results, let us summarize several key aspects. We assume that, without the impurity, the system is in a gapped (partially) polarized phase with magnons as low-energy excitations, where the magnon gap is basically set by the magnetic field, and study sub-gap magnon bound states induced by a single magnetic quantum impurity. The impurity coupling J_K now competes with the magnetic field \mathbf{h} . In a classical picture, \mathbf{h} tries to polarize all spins in the same direction, but spins coupled by J_K align in opposite directions if $J_K \gg |\mathbf{h}|$. For the adatom case with $S_{\text{imp}} = S$, the limit $J_K \rightarrow \infty$ corresponds to Kondo singlet formation between the impurity and a bulk spin, where both spins are frozen out and can be described as a vacancy. However, for the Kitaev-Heisenberg honeycomb model, a vacancy does *not* induce sub-gap bound states [37, 38]. As one varies $J_K/|\mathbf{h}|$ between the weak- and strong-coupling limits, either the impurity or the bulk spin has to flip against the magnetic field. In the adatom case with $S_{\text{imp}} \neq S$ and/or in the substitutional case, the strong-coupling limit may have a residual spin, and thus multiple transitions are possible. Below we describe such discontinuous spin transitions in the quantum case and show how they can be detected in STS.

Kitaev-Heisenberg model.—The bulk spin couplings $H_{j,k}$ in Eq. (1) include an isotropic ferromagnetic Heisenberg coupling $J_b > 0$, and a bond-dependent Kitaev contribution K . For instance, for a z -bond in Fig. 1, we have $H_{j,k} = -\text{diag}(J_b, J_b, J_b + K)$. Bulk interactions for bonds of type $\gamma \in \{x, y\}$ then follow by cyclic permutation of (α, β, γ) in $H_{j,k}^{\alpha,\beta}$. In CrI_3 , bulk spins (Cr^{3+} ions) have $S = 3/2$ [6]. Magnetic impurities at substitu-

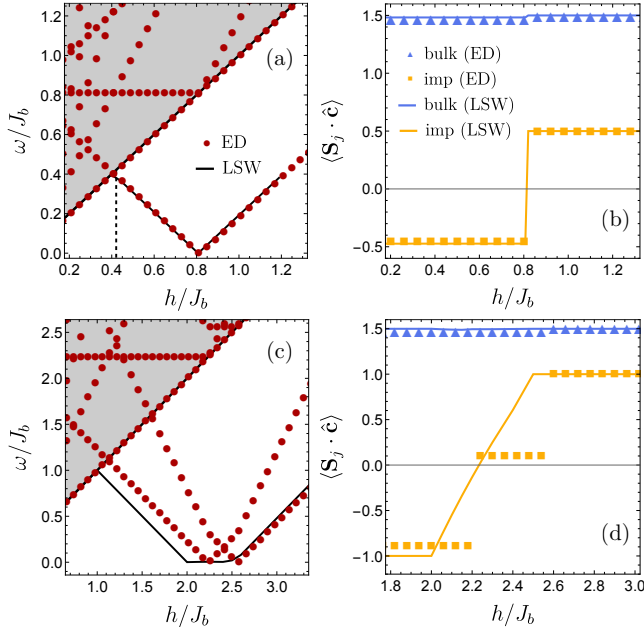


Figure 2. ED and LSW results for the Kitaev-Heisenberg model with $S = 3/2$, $K/J_b = -0.2$, $J_K/J_b = 0.5$, and $\mathbf{h} = h\hat{\mathbf{c}}$. For all cases studied here, $g = 1$ in Eq. (2). The shaded region indicates the magnon continuum $\omega > \omega_g$ in the thermodynamic limit, with the magnon gap $\omega_g = h$. ED results refer to a cluster with 2×2 unit cells (9 sites for the adatom case) and periodic boundary conditions. *Adatom impurity*: (a) Excitation spectrum ω/J_b (relative to the ground state) vs magnetic field h/J_b for $S_{\text{imp}} = 1/2$. ED (LSW) results correspond to red dots (black lines). The dashed vertical line indicates the classical spin flip transition. (b) Spin projections $\langle \mathbf{S}_{0,1} \cdot \hat{\mathbf{c}} \rangle$ vs h/J_b for the case in panel (a). Yellow squares (lines) correspond to ED (LSW) results for the impurity spin. Results for the coupled bulk spin are shown as blue triangles (ED) and blue lines (LSW), respectively. *Substitutional impurity*: (c) ω/J_b vs h/J_b and (d) $\langle \mathbf{S}_{0,1} \cdot \hat{\mathbf{c}} \rangle$ vs h/J_b for $S_{\text{imp}} = 1$.

tional sites could be, e.g., V^{3+} ions with $S_{\text{imp}} = 1$ [55] where we obtain $g = 1$ from Eq. (2). On the other hand, adatom impurities should be neutral, e.g., Co atoms with $S_{\text{imp}} = 1/2$ [22], again resulting in $g = 1$. Ab-initio calculations for CrI_3 [56] favor impurity locations in the hexagon center, while for Ni atoms, the adatom location is also possible. However, with a scanning probe tip, one can move around impurities at will [22].

We show ED and LSW results for $S = 3/2$ in Fig. 2. While ED is a numerically exact method, it is limited to small system size. LSW theory instead allows us to treat the thermodynamic limit, where the first step is to determine the classical spin configuration that minimizes the energy. In general, there can be spin canting as schematically illustrated in Fig. 1(b). One then performs a Holstein-Primakoff transformation to boson operators describing the magnons. In principle, the linearized theory becomes exact for large S [35, 36, 38, 52]. Since the

impurity breaks translation invariance, one needs to diagonalize the quadratic LSW Hamiltonian in real space. However, this can be done for fairly large lattices, allowing for an extrapolation to the thermodynamic limit. For details, see the SM [42].

Remarkably, both methods give almost perfect agreement for an adatom impurity with $S_{\text{imp}} = 1/2$, see Fig. 2(a,b). Here a sub-gap magnon bound state appears whose energy vanishes for $h/J_b \approx 0.8$. For $h \ll J_K$, the bound state merges with the magnon continuum as expected from the impurity screening scenario discussed above. As seen in Fig. 2(b), the spin projections $\langle \mathbf{S}_{0,1} \cdot \hat{\mathbf{c}} \rangle$ of the impurity spin and (to much lesser degree) the coupled bulk spin exhibit *discontinuous* jumps at $h/J_b \approx 0.8$. As we show later on, such spin transitions can be detected by STS. Importantly, the transition obtained within LSW theory is due to quantum fluctuations on top of a uniformly polarized spin configuration. By contrast, a classical transition might be expected when the energy of the configuration with the flipped impurity spin falls below the energy of the uniform configuration. Calculating these energies within LSW theory up to order S (in the $1/S$ expansion) [42], we find that this semiclassical criterion underestimates the critical magnetic field, see the dashed vertical line in Fig. 2(a).

For the adatom case and $\mathbf{h} = h\hat{\mathbf{c}}$, we can analytically determine the scaling of the sub-gap magnon bound state energy $E_b < 0$ (relative to the magnon gap ω_g) in the regime $J_K \ll h$, where Eq. (1) affords an effective continuum description [42]. In the limit of a classical magnetic impurity with $S_{\text{imp}} \rightarrow \infty$ at constant $J_K S_{\text{imp}}$ [38, 57, 58], we obtain the nonperturbative scaling law $E_b \propto -e^{-c_b/(mJ_K)}$ [59], where m parametrizes the magnon effective mass and c_b is a prefactor of order unity. However, for a quantum impurity, we find a qualitatively different scaling, $E_b \simeq gh - \omega_g - J_K S + \mathcal{O}(J_K^2)$, in accordance with our numerical ED and LSW results.

We next address the *substitutional* case for $S_{\text{imp}} = 1$, see Fig. 2(c,d), where marked differences between ED and LSW results emerge. In particular, ED results indicate *two* spin transitions associated with multiple zeros of the bound state energy. On the other hand, the LSW spectrum calculated for the uniform classical spin configuration (with polarized impurity) captures only one transition. In Fig. 2(c,d), we show the LSW spectrum and spin projections for a configuration in which the impurity spin is allowed to rotate to minimize the classical energy [42]. This continuous rotation of the impurity spin breaks the exact C_3 lattice symmetry. However, such a spontaneous symmetry breaking is not possible for a single degree of freedom with local interactions, since there are only finite energy barriers to other broken-symmetry states and quantum fluctuations can restore the symmetry. In fact, we never observed transverse components of the impurity spin in ED. Another indication of the failure of LSW theory is that the predicted magnon bound

state energy vanishes in the regime where the classical spin rotates (which is where ED identifies multiple transitions). In this case, the putative classical configuration cannot be stable because one can add magnons without energy cost. Given the excellent agreement between ED and LSW results in Fig. 2(a,b), we believe that ED captures the thermodynamic limit also in Fig. 2(c,d). The transitions at $h/J_b \approx 2.2$ and $h/J_b \approx 2.55$ are again predominantly due to discontinuities in the local magnetization. They correspond to zeros of the energy for excitations with n magnons in the bound state, where $n \leq 2S_{\text{imp}}$. For higher S_{imp} , one can thus expect more spin transitions.

STS conductance.—We next discuss how the above spin transitions can be observed in STS. In the zero-temperature limit, the STS conductance $G(V)$ at bias voltage V and tip position $\mathbf{r} = (r_x, r_y, r_z)$ can be written as [37, 38, 60–64]

$$G(V) = G_0 \sum_{j,k} \frac{t_j t_k^*}{|t_{\text{bulk}}|^2} F_{j,k}(\mathbf{r}) \sum_{\alpha} \int_0^{eV} d\omega C_{j,k}^{\alpha,\alpha}(\omega), \quad (3)$$

where $t_{j=0} = t_{\text{imp}}$ and $t_{j \neq 0} = t_{\text{bulk}}$ are cotunneling amplitudes [42]. The conductance scale is $G_0 = 2\pi d_A d_B |t_{\text{bulk}}|^2$, where d_A (d_B) is the density of states of the tip (substrate) at the Fermi level, and the factor $F_{j,k}(\mathbf{r}) = \exp\left(-\frac{|\mathbf{R}_j - \mathbf{r}| + |\mathbf{R}_k - \mathbf{r}|}{l_0}\right)$ encodes the tip position dependence. The spin sites (including the impurity) are denoted by \mathbf{R}_j , and l_0 is a length characterizing the STS resolution. Finally, the dynamical spin correlation function is given by $C_{j,k}^{\alpha,\beta}(\omega) = \int dt e^{i\omega t} \langle S_j^{\alpha}(t) S_k^{\beta}(0) \rangle$, using the ground state of Eq. (1). We note that on top of the inelastic contribution (3), there is a featureless voltage-independent elastic cotunneling term [38, 62]. For finite bound state energy, the zero-bias conductance obtained from Eq. (3) is expressed in terms of spin expectation values $\langle S_j^{\alpha} \rangle$ only,

$$G(V=0) = G_0 \sum_{\alpha} \left| \sum_j \frac{t_j}{|t_{\text{bulk}}|} e^{-|\mathbf{R}_j - \mathbf{r}|/l_0} \langle S_j^{\alpha} \rangle \right|^2, \quad (4)$$

such that discontinuous spin transitions are directly visible as conductance steps.

We illustrate the above results in Fig. 3 for an adatom impurity with $S_{\text{imp}} = 1/2$, cf. Fig. 2(a,b). The step in the field dependence of the zero-bias conductance seen in Fig. 3(a) directly follows from the spin transition in Fig. 2(b) through Eq. (4). One can therefore use the zero-bias STS conductance to monitor the above spin transitions. At low but finite bias voltage, Fig. 3(b) illustrates that the conductance derivative dG/dV exhibits a pronounced *peak* whenever the voltage matches the sub-gap magnon bound state energy. By varying both the magnetic field and the bias voltage, one can thus map out the complete field dependence of the bound state energy in

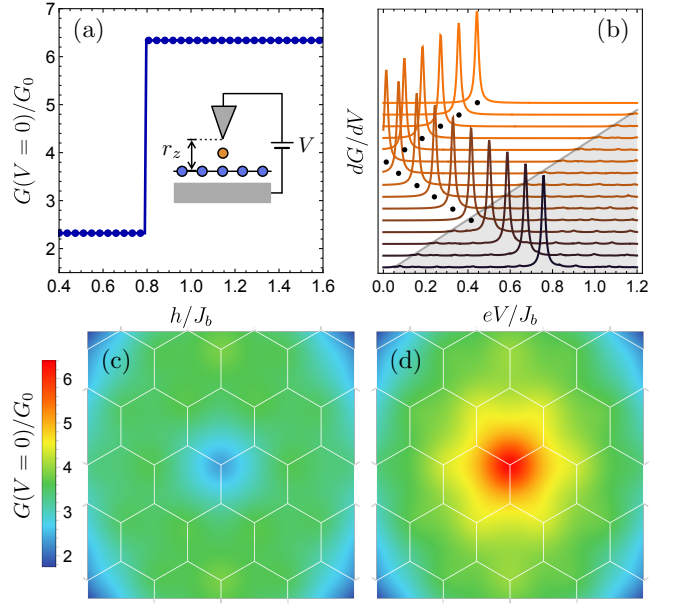


Figure 3. STS conductance for the Kitaev-Heisenberg model with an adatom magnetic impurity from LSW theory, cf. Fig. 2(a,b), with $K = -0.2J_b$, $J_K = 0.5J_b$, $S = 3/2$, $S_{\text{imp}} = 1/2$, and $g = 1$. The STM tip and the impurity position, see Eq. (3), are characterized by $l_0 = r_z = 0.5a_0$, $t_{\text{imp}}/t_{\text{bulk}} = 1.5$, and $\mathbf{R}_0 = \mathbf{R}_1 + 0.2a_0\hat{c}$, where a_0 is the lattice constant and $j = 1$ indicates the bulk spin coupled to the impurity. (a) Zero-bias conductance (4) vs magnetic field h for a tip above the impurity as schematically depicted in the inset. (b) Conductance derivative dG/dV (in arbitrary units) vs bias voltage. Different curves correspond to uniformly spaced field values ranging from $h = 0.05J_b$ (bottom) to $h = 1.25J_b$ (top curve), shifted vertically to aid visualization. The δ -function peaks have been broadened by a Lorentzian of width $0.01J_b$. The dots track the bound state energy. (c,d) Color-scale plots for the spatial profile of the zero-bias conductance near the magnetic impurity (which is in the center of the respective panel) for two field values: (c) $h = 0.65J_b$ (below the transition), (d) $h = 1.164J_b$ (above the transition).

STS. Finally, as illustrated in Fig. 3(c,d), by scanning the zero-bias conductance in the vicinity of the impurity, we find that the conductance switches from a minimum to a maximum near the impurity site when increasing h/J_b across the transition at $h/J_b \approx 0.8$. This finding is also consistent with the results shown in Fig. 3(a).

Conclusions.—Depending on the parameter regime, magnetic impurities in 2D magnets can give rise to magnon bound states at very low energies. Such states might mimic the behavior of fractional excitations such as spinons or \mathbb{Z}_2 vortices in more exotic scenarios. In order to distinguish such phases, one could characterize magnon bound states by STS by first exposing the system to a strong field. In a second step, one lowers the magnetic field in order to reach the putative quantum spin liquid phase, where STS predictions are also available

[38, 63, 64]. In any case, we expect that the predicted spin transitions due to zero-energy magnon bound states will soon be observed in 2D magnets.

We acknowledge funding by the Deutsche Forschungsgemeinschaft (DFG, German Research Foundation), Projektnummer 277101999 - TRR 183 (project C01) and under Germany's Excellence Strategy - Cluster of Excellence Matter and Light for Quantum Computing (ML4Q) EXC 2004/1 - 390534769, by the Simons Foundation (Grant No. 1023171, R.G.P.), by the Brazilian ministries MEC and MCTI, by the Brazilian agencies CNPq and FAPESP, and by the Coordenação de Aperfeiçoamento de Pessoal de Nível Superior - Brasil (CAPES) - Finance Code 001.

-
- [1] K. S. Burch, D. Mandrus, and J.-G. Park, Magnetism in two-dimensional van der Waals materials, *Nature* **563**, 47 (2018).
 - [2] M. Gibertini, M. Koperski, A. F. Morpurgo, and K. S. Novoselov, Magnetic 2D materials and heterostructures, *Nat. Nanotechnol.* **14**, 408 (2019).
 - [3] Y. Khan, S. M. Obaidulla, M. R. Habib, A. Gayen, T. Liang, X. Wang, and M. Xu, Recent breakthroughs in two-dimensional van der Waals magnetic materials and emerging applications, *Nano Today* **34**, 100902 (2020).
 - [4] S. Yang, T. Zhang, and C. Jiang, Van der Waals Magnets: Material Family, Detection and Modulation of Magnetism, and Perspective in Spintronics, *Adv. Sci.* **8**, 2002488 (2021).
 - [5] H. Kurebayashi, J. H. Garcia, S. Khan, J. Sinova, and S. Roche, Magnetism, symmetry and spin transport in van der Waals layered systems, *Nat. Rev. Phys.* **4**, 150 (2022).
 - [6] Q. H. Wang, A. Bedoya-Pinto, M. Blei, A. H. Dismukes, A. Hamo, S. Jenkins, M. Koperski, Y. Liu, Q.-C. Sun, E. J. Telford, H. H. Kim, M. Augustin, U. Vool, J.-X. Yin, L. H. Li, A. Falin, C. R. Dean, F. Casanova, R. F. L. Evans, M. Chshiev, A. Mishchenko, C. Petrovic, R. He, L. Zhao, A. W. Tsen, B. D. Gerardot, M. Brotons-Gisbert, Z. Guguchia, X. Roy, S. Tongay, Z. Wang, M. Z. Hasan, J. Wrachtrup, A. Yacoby, A. Fert, S. Parkin, K. S. Novoselov, P. Dai, L. Balicas, and E. J. G. Santos, The Magnetic Genome of Two-Dimensional van der Waals Materials, *ACS Nano* **16**, 6960 (2022).
 - [7] Y. Ahn, X. Guo, S. Son, Z. Sun, and L. Zhao, Progress and Prospects in Two-Dimensional Magnetism of van der Waals Materials (2024), [arXiv:2401.13781 \[cond-mat.mtrl-sci\]](https://arxiv.org/abs/2401.13781).
 - [8] J.-X. Yin, S. H. Pan, and M. Z. Hasan, Probing topological quantum matter with scanning tunneling microscopy, *Nat. Rev. Phys.* **3**, 249 (2021).
 - [9] A. J. Heinrich, J. A. Gupta, C. P. Lutz, and D. M. Eigler, Single-Atom Spin-Flip Spectroscopy, *Science* **306**, 466 (2004).
 - [10] R. Wiesendanger, Spin mapping at the nanoscale and atomic scale, *Rev. Mod. Phys.* **81**, 1495 (2009).
 - [11] B. Huang, G. Clark, E. Navarro-Moratalla, D. R. Klein, R. Cheng, K. L. Seyler, D. Zhong, E. Schmidgall, M. A. McGuire, D. H. Cobden, W. Yao, D. Xiao, P. Jarillo-Herrero, and X. Xu, Layer-dependent ferromagnetism in a van der Waals crystal down to the monolayer limit, *Nature* **546**, 270 (2017).
 - [12] J. L. Lado and J. Fernández-Rossier, On the origin of magnetic anisotropy in two dimensional CrI₃, *2D Materials* **4**, 035002 (2017).
 - [13] L. Chen, J.-H. Chung, T. Chen, C. Duan, A. Schneidewind, I. Radelytskyi, D. J. Voneshen, R. A. Ewings, M. B. Stone, A. I. Kolesnikov, B. Winn, S. Chi, R. A. Mole, D. H. Yu, B. Gao, and P. Dai, Magnetic anisotropy in ferromagnetic CrI₃, *Phys. Rev. B* **101**, 134418 (2020).
 - [14] I. Lee, F. G. Utermohlen, D. Weber, K. Hwang, C. Zhang, J. van Tol, J. E. Goldberger, N. Trivedi, and P. C. Hammel, Fundamental spin interactions underlying the magnetic anisotropy in the kitaev ferromagnet CrI₃, *Phys. Rev. Lett.* **124**, 017201 (2020).
 - [15] L. Chen, J.-H. Chung, M. B. Stone, A. I. Kolesnikov, B. Winn, V. O. Garlea, D. L. Abernathy, B. Gao, M. Augustin, E. J. G. Santos, and P. Dai, Magnetic Field Effect on Topological Spin Excitations in CrI₃, *Phys. Rev. X* **11**, 031047 (2021).
 - [16] P. P. Stavropoulos, X. Liu, and H.-Y. Kee, Magnetic anisotropy in spin-3/2 with heavy ligand in honeycomb Mott insulators: Application to CrI₃, *Phys. Rev. Res.* **3**, 013216 (2021).
 - [17] S. M. Winter, A. A. Tsirlin, M. Daghofer, J. van den Brink, Y. Singh, P. Gegenwart, and R. Valentí, Models and materials for generalized Kitaev magnetism, *J. Phys.: Condens. Matter* **29**, 493002 (2017).
 - [18] J. Knolle and R. Moessner, A Field Guide to Spin Liquids, *Annu. Rev. Condens. Matter Phys.* **10**, 451 (2019).
 - [19] C. Hickey, M. Gohlke, C. Berke, and S. Trebst, Generic field-driven phenomena in Kitaev spin liquids: Canted magnetism and proximate spin liquid physics, *Phys. Rev. B* **103**, 064417 (2021).
 - [20] I. Rouschatzakis, N. B. Perkins, Q. Luo, and H.-Y. Kee, Beyond Kitaev physics in strong spin-orbit coupled magnets, *Rep. Prog. Phys.* **87**, 026502 (2024).
 - [21] S. Lee, Y. S. Choi, S.-H. Do, W. Lee, C. H. Lee, M. Lee, M. Vojta, C. N. Wang, H. Luetkens, Z. Guguchia, and K.-Y. Choi, Kondo screening in a Majorana metal, *Nat. Commun.* **14**, 7405 (2023).
 - [22] Y. Chen, W.-Y. He, W. Ruan, J. Hwang, S. Tang, R. L. Lee, M. Wu, T. Zhu, C. Zhang, H. Ryu, F. Wang, S. G. Louie, Z.-X. Shen, S.-K. Mo, P. A. Lee, and M. F. Crommie, Evidence for a spinon Kondo effect in cobalt atoms on single-layer 1T - TaSe₂, *Nat. Phys.* **18**, 1335 (2022).
 - [23] W.-Y. He and P. A. Lee, Magnetic impurity as a local probe of the U(1) quantum spin liquid with spinon Fermi surface, *Phys. Rev. B* **105**, 195156 (2022).
 - [24] P. Kattel, P. R. Pasnoori, J. H. Pixley, P. Azaria, and N. Andrei, Kondo effect in the isotropic Heisenberg spin chain, *Phys. Rev. B* **109**, 174416 (2024).
 - [25] S. Mishra, G. Catarina, F. Wu, R. Ortiz, D. Jacob, K. Eimre, J. Ma, C. A. Pignedoli, X. Feng, P. Ruffieux, F. Fernández-Rossier, and R. Fasel, Observation of fractional edge excitations in nanographene spin chains, *Nature* **598**, 287 (2021).
 - [26] D. Jacob, R. Ortiz, and J. Fernández-Rossier, Renormalization of spin excitations and Kondo effect in open-shell nanographenes, *Phys. Rev. B* **104**, 075404 (2021).
 - [27] A. Kitaev, Anyons in an exactly solved model and beyond, *Ann. Phys.* **321**, 2 (2006).

- [28] L. Savary and L. Balents, Quantum spin liquids: a review, *Rep. Prog. Phys.* **80**, 016502 (2016).
- [29] Y. Zhou, K. Kanoda, and T.-K. Ng, Quantum spin liquid states, *Rev. Mod. Phys.* **89**, 025003 (2017).
- [30] M. Hermanns, I. Kimchi, and J. Knolle, Physics of the Kitaev model: Fractionalization, dynamic correlations, and material connections, *Annu. Rev. Condens. Matter. Phys.* **9**, 17 (2018).
- [31] H. Takagi, T. Takayama, G. Jackeli, G. Khaliullin, and S. E. Nagler, Concept and realization of Kitaev quantum spin liquids, *Nat. Rev. Phys.* **1**, 264 (2019).
- [32] Y. Motome and J. Nasu, Hunting Majorana fermions in Kitaev magnets, *J. Phys. Soc. Jpn.* **89**, 012002 (2020).
- [33] S. Trebst and C. Hickey, Kitaev materials, *Phys. Rep.* **950**, 1 (2022).
- [34] P. A. McClarty, X.-Y. Dong, M. Gohlke, J. G. Rau, F. Pollmann, R. Moessner, and K. Penc, Topological magnons in Kitaev magnets at high fields, *Phys. Rev. B* **98**, 060404 (2018).
- [35] L. E. Chern, E. Z. Zhang, and Y. B. Kim, Sign structure of thermal Hall conductivity and topological magnons for in-plane field polarized Kitaev magnets, *Phys. Rev. Lett.* **126**, 147201 (2021).
- [36] E. Z. Zhang, L. E. Chern, and Y. B. Kim, Topological magnons for thermal Hall transport in frustrated magnets with bond-dependent interactions, *Phys. Rev. B* **103**, 174402 (2021).
- [37] A. Mitra, A. Corticelli, P. Ribeiro, and P. A. McClarty, Magnon Interference Tunneling Spectroscopy as a Probe of 2D Magnetism, *Phys. Rev. Lett.* **130**, 066701 (2023).
- [38] T. Bauer, L. R. D. Freitas, R. G. Pereira, and R. Egger, Scanning tunneling spectroscopy of Majorana zero modes in a Kitaev spin liquid, *Phys. Rev. B* **107**, 054432 (2023).
- [39] R.-J. Slager, L. Rademaker, J. Zaanen, and L. Balents, Impurity-bound states and Green's function zeros as local signatures of topology, *Phys. Rev. B* **92**, 085126 (2015).
- [40] S.-S. Diop, L. Fritz, M. Vojta, and S. Rachel, Impurity bound states as detectors of topological band structures revisited, *Phys. Rev. B* **101**, 245132 (2020).
- [41] J. Habel, A. Mook, J. Willsher, and J. Knolle, Breakdown of chiral edge modes in topological magnon insulators, *Phys. Rev. B* **109**, 024441 (2024).
- [42] See the Online Supplementary Material (SM), where we provide details on our derivations and additional data.
- [43] L. Janssen and M. Vojta, Heisenberg-Kitaev physics in magnetic fields, *J. Phys. Condens. Matter* **31**, 423002 (2019).
- [44] J. Villain, Insulating spin glasses, *Z. Phys. B* **33**, 31 (1979).
- [45] A. Wollny, L. Fritz, and M. Vojta, Fractional Impurity Moments in Two-Dimensional Noncollinear Magnets, *Phys. Rev. Lett.* **107**, 137204 (2011).
- [46] A. Wollny, E. C. Andrade, and M. Vojta, Singular field response and singular screening of vacancies in antiferromagnets, *Phys. Rev. Lett.* **109**, 177203 (2012).
- [47] V. S. Maryasin and M. E. Zhitomirsky, Triangular antiferromagnet with nonmagnetic impurities, *Phys. Rev. Lett.* **111**, 247201 (2013).
- [48] J. G. Rau and M. J. P. Gingras, Frustration and anisotropic exchange in ytterbium magnets with edge-shared octahedra, *Phys. Rev. B* **98**, 054408 (2018).
- [49] C. Xu, J. Feng, H. Xiang, and L. Bellaiche, Interplay between Kitaev interaction and single ion anisotropy in ferromagnetic CrI_3 and CrGeTe_3 monolayers, *npj Comput. Mater.* **4**, 57 (2018).
- [50] R. Jaeschke-Ubiergo, E. Suárez Morell, and A. S. Nunez, Theory of magnetism in the van der Waals magnet CrI_3 , *Phys. Rev. B* **103**, 174410 (2021).
- [51] J. Cen and H.-Y. Kee, Determining Kitaev interaction in spin- S honeycomb Mott insulators, *Phys. Rev. B* **107**, 014411 (2023).
- [52] P. Fazekas, *Lecture Notes on Electron Correlation and Magnetism* (World Scientific, 1999).
- [53] G. Jackeli and G. Khaliullin, Mott Insulators in the Strong Spin-Orbit Coupling Limit: From Heisenberg to a Quantum Compass and Kitaev Models, *Phys. Rev. Lett.* **102**, 017205 (2009).
- [54] S. M. Winter, K. Riedl, D. Kaib, R. Coldea, and R. Valentí, Probing $\alpha\text{-RuCl}_3$ Beyond Magnetic Order: Effects of Temperature and Magnetic Field, *Phys. Rev. Lett.* **120**, 077203 (2018).
- [55] S. Son, M. J. Coak, N. Lee, J. Kim, T. Y. Kim, H. Hamidov, H. Cho, C. Liu, D. M. Jarvis, P. A. C. Brown, J. H. Kim, C.-H. Park, D. I. Khomskii, S. S. Saxena, and J.-G. Park, Bulk properties of the van der Waals hard ferromagnet VI_3 , *Phys. Rev. B* **99**, 041402 (2019).
- [56] Q. Yang, X. Hu, X. Shen, A. V. Krasheninnikov, Z. Chen, and L. Sun, Enhancing Ferromagnetism and Tuning Electronic Properties of CrI_3 Monolayers by Adsorption of Transition-Metal Atoms, *ACS Applied Materials & Interfaces* **13**, 21593 (2021).
- [57] H. Shiba, Classical Spins in Superconductors, *Prog. Theor. Phys.* **40**, 435 (1968).
- [58] Y. Imry and S.-k. Ma, Random-Field Instability of the Ordered State of Continuous Symmetry, *Phys. Rev. Lett.* **35**, 1399 (1975).
- [59] R. Jackiw, Delta function potentials in two-dimensional and three-dimensional quantum mechanics, in *M.A.B. Bég Memorial Volume*, edited by A. Ali and P. Hoodbhoy (World Scientific, Singapore, 1991).
- [60] J. Fransson, O. Eriksson, and A. Balatsky, Theory of spin-polarized scanning tunneling microscopy applied to local spins, *Phys. Rev. B* **81**, 115454 (2010).
- [61] J. Fernández-Rossier, Theory of single-spin inelastic tunneling spectroscopy, *Phys. Rev. Lett.* **102**, 256802 (2009).
- [62] J. Feldmeier, W. Natori, M. Knap, and J. Knolle, Local probes for charge-neutral edge states in two-dimensional quantum magnets, *Phys. Rev. B* **102**, 134423 (2020).
- [63] W.-H. Kao, N. B. Perkins, and G. B. Halász, Vacancy Spectroscopy of Non-Abelian Kitaev Spin Liquids, *Phys. Rev. Lett.* **132**, 136503 (2024).
- [64] W.-H. Kao, G. B. Halász, and N. B. Perkins, Dynamics of vacancy-induced modes in the non-Abelian Kitaev spin liquid, *Phys. Rev. B* **109**, 125150 (2024).

Supplemental Material

We here provide (i) details about linear spin wave theory in the presence of a single magnetic quantum impurity, (ii) derive analytical results for the sub-gap magnon bound state energy in the weak-coupling limit, (iii) give additional background on the tunneling conductance expression, and (iv) show data for the idealized Kitaev honeycomb model. Equation (X) in the main text is referred to as Eq. (MX) below.

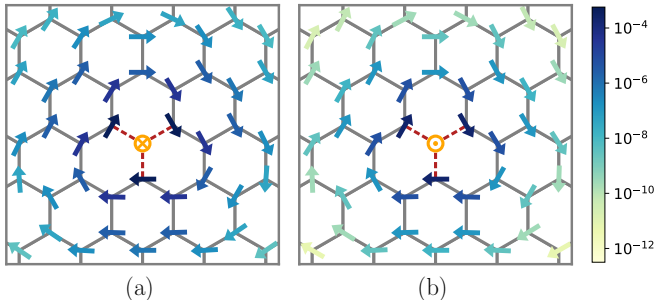


Figure 4. Examples for classical spin configurations near a magnetic impurity of substitution type in the Kitaev-Heisenberg model. Arrows represent spin components in the ab plane, where the color scale indicates the magnitude of the in-plane component. Orange-colored symbols show the out-of-plane components of the impurity spin. Parameters are chosen as in Fig. 2(c) of the main text, i.e., $S = 3/2$, $S_{\text{imp}} = 1/2$, $K/J_b = -0.2$, and $J_K/J_b = 0.5$. Panel (a) shows results for $h/J_b = 1.2$, i.e., below the spin transitions. Panel (b) is for $h/J_b = 3.5$, i.e., above the spin transitions.

I. LSW theory

As one method for studying partially polarized phases of 2D magnets with a single magnetic quantum impurity, see Eq. (M1), we use LSW theory [52]. One starts by determining the classical spin configuration minimizing the energy, see Sec. IA. After rotating the local spin quantization axis to the corresponding classical spin axis, one performs a Holstein-Primakoff transformation to introduce boson operators for the magnon degrees of freedom. We consider a linear approximation, where the Hamiltonian can be diagonalized by a Bogoliubov transformation, see Sec. IB. In Sec. IC, we briefly describe how one can obtain dynamical spin correlations from this approach, which enter the STS conductance (M3). In Sec. ID, we discuss estimates for the regime where discontinuous spin transitions occur based on comparing the energies of the competing classical configurations.

A. Classical spin configuration and spin canting

The first step is to find the classical spin configuration that minimizes the energy. In frustrated magnets, inhomogeneities can locally tip the energy balance and disturb the local spin environment, a phenomenon dubbed local relief of frustration [44]. Because a classical adatom magnetic impurity effectively acts as a local field, a local distortion (“spin canting”, schematically illustrated in Fig. 1(b) of the main text) occurs in the neighboring bulk spins with respect to the uniform case. For a substitutional impurity, the situation is similar, as the bulk spins neighboring the impurity feel an imbalance in their local exchange field. In noncollinear long-ranged

ordered phases, such local distortions decay as a power law in space and lead to nontrivial spin textures [45–47]. In polarized phases, magnons are gapped and we expect an exponential decay of the texture, limiting it to the immediate vicinity of the impurity. We numerically determine the classical ground state by sequentially anti-aligning the spins with their local exchange field. To ensure convergence, we start from distinct initial conditions and select as the ground state the spin texture with the lowest energy. This procedure allows us to obtain canted spin texture and gauge the competition between the impurity-bulk exchange coupling $J_K > 0$ and the external magnetic field strength h in determining the local spin configuration.

As an example, we show results for the Kitaev-Heisenberg honeycomb model with a substitutional magnetic impurity. Figure 4 illustrates the classical spin configuration for the same parameters as in Fig. 2(c) of the main text. Here we choose two values of the magnetic field along the \hat{c} direction, where the impurity spin in the classical configuration is either antiparallel [Fig. 4(a)] or parallel [Fig. 4(b)] to the field direction. This way, we avoid the regime near the transitions where the classical state incorrectly predicts a smooth rotation of the impurity spin. As shown in Fig. 4, we observe a vortex-like pattern for the bulk spin components in the ab plane, both above and below the transition. In contrast to the spurious rotation of the impurity spin discussed in the main text, the vortex-like pattern for the bulk spins respects the discrete \mathbb{Z}_3 spin-rotation symmetry around the impurity site. A similar pattern has been observed near a vacancy in the Kitaev-Heisenberg model [37].

B. Holstein-Primakoff transformation

Given the classical spin configuration, we apply a local rotation that aligns the z -axis with the local spin polarization, $\mathbf{S}_j = R_j \hat{\mathbf{S}}_j$, where R_j is an orthogonal matrix. For polarized phases with a homogeneous spin configuration, $R_j = R$ is site independent and there is no spin canting. For instance, assuming that all spins are polarized by a magnetic field perpendicular to the honeycomb plane, $\mathbf{h} = h\hat{c}$, the spin basis used for representing the Kitaev-Heisenberg honeycomb model is rotated according to [27]

$$R = \begin{pmatrix} \frac{1}{\sqrt{6}} & \frac{-1}{\sqrt{2}} & \frac{1}{\sqrt{3}} \\ \frac{1}{\sqrt{6}} & \frac{1}{\sqrt{2}} & \frac{1}{\sqrt{3}} \\ \frac{-2}{\sqrt{6}} & \frac{1}{\sqrt{2}} & \frac{1}{\sqrt{3}} \end{pmatrix}. \quad (5)$$

In any case, given the orthogonal matrices R_j , we next employ a standard Holstein-Primakoff transformation in order to represent spin operators in terms of bosonic op-

erators b_j and b_j^\dagger describing magnons [52],

$$\begin{aligned}\tilde{S}_j^z &= S_j - n_j, & \tilde{S}_j^+ &= \sqrt{2S_j - n_j} b_j \approx \sqrt{2S_j} b_j, \\ \tilde{S}_j^- &= b_j^\dagger \sqrt{2S_j - n_j} \approx \sqrt{2S_j} b_j^\dagger,\end{aligned}\quad (6)$$

where $n_j = b_j^\dagger b_j$. The polarized impurity spin at $j = 0$ is included in Eq. (6), where $S_0 = S_{\text{imp}}$ generally differs from the value for bulk spins, $S_{j \neq 0} = S$.

To leading order in $1/S$, the Hamiltonian can be written as

$$H = E_{\text{cl}} + H_{\text{sw}} + \mathcal{O}(S^{1/2}), \quad (7)$$

where $E_{\text{cl}} \sim \mathcal{O}(S^2)$ is the classical ground state energy and $H_{\text{sw}} \sim \mathcal{O}(S)$ is the LSW Hamiltonian,

$$H_{\text{sw}} = \sum_{\langle j,k \rangle} \left[t_{j,k} b_j^\dagger b_k + \Delta_{j,k} b_j b_k + \text{h.c.} \right] + \sum_j h_j^{\text{eff}} b_j^\dagger b_j. \quad (8)$$

For $S \rightarrow \infty$, the LSW approach, neglecting all terms beyond H_{sw} in Eq. (7), becomes formally exact (but see below and the main text for subtleties related to the classical reference configuration). The parameters $t_{j,k}$ and $\Delta_{j,k}$ in Eq. (8) follow from the rotated spin-spin interaction matrices, $\tilde{H}_{j,k} = R_j^T H_{j,k} R_k$ with $H_{j,k}$ in Eq. (M1), as

$$\begin{aligned}t_{j,k} &= \frac{\sqrt{S_j S_k}}{2} \left[\left(\tilde{H}_{j,k}^{xx} - i \tilde{H}_{j,k}^{xy} \right) + \left(\tilde{H}_{j,k}^{yy} + i \tilde{H}_{j,k}^{yx} \right) \right], \\ \Delta_{j,k} &= \frac{\sqrt{S_j S_k}}{2} \left[\left(\tilde{H}_{j,k}^{xx} - i \tilde{H}_{j,k}^{xy} \right) - \left(\tilde{H}_{j,k}^{yy} + i \tilde{H}_{j,k}^{yx} \right) \right]\end{aligned}\quad (9)$$

Note that the anomalous couplings $\Delta_{j,k}$ change the total number of magnons. The effective field h_j^{eff} involves both the external field and a contribution from spin interactions. For bulk sites ($j \neq 0$), we find

$$h_j^{\text{eff}} = \tilde{h}^z - \sum_{k \in \mathcal{V}_j} S_k \tilde{H}_{j,k}^{zz}, \quad (10)$$

where \mathcal{V}_j denotes the set of nearest neighbors of j and \tilde{h}^z is the z -component of the rotated field $\tilde{\mathbf{h}} = R_j^T \mathbf{h}$. At the impurity site ($j = 0$), the effective field is given by

$$h_0^{\text{eff}} = g \tilde{h}^z - \sum_{k \in \mathcal{V}_0} S \tilde{H}_{j,k}^{zz} = g h - |\mathcal{V}_0| S J_K, \quad (11)$$

where $|\mathcal{V}_0| = 1$ for an adatom and $|\mathcal{V}_0| = 3$ for a substitutional impurity. The second equality only holds for a polarized uniform spin configuration, where $\tilde{h}^z = h$. The factor g has been defined in Eq. (M2).

The quadratic Hamiltonian (8) can be diagonalized by a Bogoliubov transformation. For a decoupled adatom impurity ($J_K = 0$) and a fully polarized system, we can diagonalize the Hamiltonian in momentum space and obtain analytical expressions for the magnon dispersion

relation. The magnon gap is given by $\omega_g = h$ for the Kitaev-Heisenberg model. For $J_K > 0$, we perform a Bogoliubov transformation in real space for a finite system with periodic boundary conditions, and then extrapolate to the thermodynamic limit.

As shown in Fig. 2 of the main text, sub-gap magnon bound states appear for arbitrarily small exchange coupling $J_K > 0$. Within LSW theory, the discontinuous spin transition is well described by calculating $\langle \tilde{S}_j^z \rangle = S_j - \langle b_j^\dagger b_j \rangle$ for the adatom case in the uniform classical configuration. Even without changing the classical state, the discontinuity in the quantum correction to the magnetization is possible because there is a rearrangement of the eigenvectors in the Bogoliubov transformation when the lowest eigenvalue (associated with the magnon bound state) goes through zero.

C. Dynamical spin correlations

Let us briefly sketch how to obtain dynamical spin correlations from this approach. The Bogoliubov transformation yields the single-particle eigenenergies ω_n with bosonic eigenoperators \tilde{b}_n and \tilde{b}_n^\dagger . We can thereby rewrite Eq. (8) as

$$H_{\text{sw}} = \sum_n \omega_n \tilde{b}_n^\dagger \tilde{b}_n + \Delta E, \quad \Delta E = \frac{1}{2} \sum_n \omega_n. \quad (12)$$

The Lehmann representation of the dynamical spin correlations appearing in the STS conductance expression (M3) is given by

$$C_{jk}^{\alpha\beta}(\omega) = \sum_\nu \langle \Phi_0 | S_j^\alpha | \Phi_\nu \rangle \langle \Phi_\nu | S_k^\beta | \Phi_0 \rangle \delta(\omega + E_0 - E_\nu), \quad (13)$$

where $|\Phi_\nu\rangle$ are many-body eigenstates with energy E_ν , including the ground state $|\Phi_0\rangle$ with energy E_0 . Within LSW theory, the matrix elements $\langle \Phi_0 | S_j^\alpha | \Phi_\nu \rangle$ are finite only for states of the form

$$|\Phi_\nu\rangle \propto |\Phi_0\rangle, \quad |\Phi_\nu\rangle \propto \tilde{b}_n^\dagger |\Phi_0\rangle \quad \text{or} \quad |\Phi_\nu\rangle \propto \tilde{b}_n^\dagger \tilde{b}_m^\dagger |\Phi_0\rangle. \quad (14)$$

We can thereby rationalize the emergence of zero-, one- and two-magnon contributions in the nonlinear STS conductance. However, we find that the two-magnon contribution of the bound state vanishes within LSW theory. For the pure Heisenberg model ($K = 0$) in a perpendicular magnetic field above the transition, i.e., for $h \gg J_K$, this follows analytically from magnon number conservation, i.e., $\Delta_{j,k} = 0$ in Eq. (9). This fact implies that spin expectation values do not fluctuate for magnetic fields above the spin flip transition within LSW theory. This analytical argument does not hold below the transition or for finite Kitaev interaction, but we here have verified the absence of two-magnon contributions numerically.

D. Classical spin flip

In the main text, we mentioned that LSW theory provides an estimate for a classical spin flip transition. At strong magnetic fields, $h \gg J_K$, the classical ground state is homogeneous and fully polarized. On the other hand, as we decrease the ratio h/J_K , at some point a spin flip will be energetically preferred in the classical ground state configuration. The energy cost of flipping the spin at site j is given by $2S_j h_j^{\text{eff}}$, with the effective field in Eq. (10) for a bulk spin and in Eq. (11) for the impurity. For an adatom impurity, the classical configuration with a flipped spin has lower energy than the uniform classical state if the magnetic field falls below the critical value $h^* = \max(h_{\text{imp}}^*, h_{\text{bulk}}^*)$, where

$$h_{\text{imp}}^* = \frac{S}{g} J_K, \quad h_{\text{bulk}}^* = \sum_{k \in \mathcal{V}_{j'}} S_k \tilde{H}_{j',k}^{zz} \quad (15)$$

correspond to a spin flip of the impurity and the bulk spin $j' \in \mathcal{V}_0$ coupled to the impurity, respectively. Note that for $g \gg 1$, we have $h^* = h_{\text{bulk}}^*$, meaning that in this case we expect the bulk spin to flip against the magnetic field as we decrease h/J_K .

Applying Eq. (15) for an adatom impurity with $S_{\text{imp}} = 1/2$ and the same parameters as in Fig. 2(a,b) of the main text, we obtain the estimate $h^*/J_b \simeq 0.75$ for the classical spin flip transition. However, this estimate is based on comparing the classical energies at order S^2 . If we include quantum corrections to the ground state energy only at order S , the estimate for the classical spin flip shifts to the much smaller value $h^*/J_b \simeq 0.42$, indicated as dashed vertical line in Fig. 2(a) of the main text. Moreover, the latter estimate neglects a possible spin canting in the classical configuration near the flipped spin. (In the adatom case, this can only happen if the bulk spin is flipped.) We stress that, while this semiclassical analysis tells us that a spin flip must occur as we decrease h/J_K , the comparison with ED indicates that the discontinuous spin transition of a $S_{\text{imp}} = 1/2$ magnetic impurity is better described by quantum fluctuations on top of the uniform spin configuration.

II. Analytical results for bound state energies

In this section, we consider an adatom impurity position and a perpendicular magnetic field, $\mathbf{h} = \hat{\mathbf{c}}$. We study the Kitaev-Heisenberg model in the weak-coupling limit $J_K \ll h$. In this case, there is no spin canting and we stay away from spin transitions. Our goal is to obtain analytical results for the sub-gap magnon bound state energy.

Under the above conditions, we can treat the adatom as a weak perturbation to the homogeneous system. We take the continuum limit of the LSW Hamiltonian (8)

by expanding the free magnon spectrum about the band minimum at the Γ point. The magnon dispersion is then approximated by $\omega(\mathbf{k}) \approx \omega_g + \frac{\mathbf{k}^2}{2m}$, where ω_g is the magnon gap and the mass term is isotropic. For the Kitaev-Heisenberg model, we find $\omega_g = h$ and

$$m^{-1} = J + \frac{K}{3} - \frac{K^2}{h + 3J + K}. \quad (16)$$

We recall that for $K \neq 0$, magnon number is not conserved, see Eq. (8). In the unperturbed free-magnon Hamiltonian, this effect is taken care of by the Bogoliubov transformation that gives the magnon dispersion to order k^2 . Next, we take the continuum limit of the impurity contribution, where we expand the bulk modes in terms of momentum eigenstates and neglect terms beyond zeroth order in k . As a result, the Kondo interaction and the Zeeman term for the impurity spin give

$$\begin{aligned} H_{\text{imp}} = & -J_K S_{\text{imp}} b^\dagger(\mathbf{R}_1) b(\mathbf{R}_1) \\ & + J_K \sqrt{S S_{\text{imp}}} [b^\dagger(\mathbf{R}_0) b(\mathbf{R}_1) + \text{h.c.}] \\ & + (gh - S J_K) b^\dagger(\mathbf{R}_0) b(\mathbf{R}_0) + \text{const.}, \end{aligned} \quad (17)$$

where $b(\mathbf{R})$ annihilates a boson at position \mathbf{R} , with \mathbf{R}_0 and \mathbf{R}_1 being the positions of the impurity and the bulk spin coupled to the impurity, respectively. We single out the impurity mode by introducing the notation $a = b(\mathbf{R}_0)$, whereas all the bulk modes are represented by $b(\mathbf{r})$ with $\mathbf{r} \in \mathbb{R}^2$ a vector in the plane that contains the honeycomb lattice. Setting $\mathbf{R}_1 = 0$ and measuring the energies with respect to the lower threshold ω_g of the magnon continuum, we write the effective low-energy Hamiltonian in real space as

$$\begin{aligned} H_{\text{eff}} = & \int d^2 r b^\dagger(\mathbf{r}) \left[-\frac{\nabla^2}{2m} - V_0 \delta(\mathbf{r}) \right] b(\mathbf{r}) \\ & + \varepsilon_a a^\dagger a + w [a^\dagger b(\mathbf{r}=0) + b^\dagger(\mathbf{r}=0) a]. \end{aligned} \quad (18)$$

Here, $V_0 = J_K S_{\text{imp}}$ is the strength of an attractive potential for the bulk magnons induced by the magnetization of the impurity. The energy of the bosonic state associated with the impurity (measured from the bulk magnon gap ω_g) is

$$\varepsilon_a = gh - \omega_g - J_K S. \quad (19)$$

Note that the occupation $a^\dagger a$ of this state can change due to quantum fluctuations of the impurity. Finally, $w = J_K \sqrt{S S_{\text{imp}}}$ is an effective hybridization due to the transverse part of the Kondo interaction. The classical magnetic impurity limit [38, 58] corresponds to taking $S_{\text{imp}} \rightarrow \infty$ and $J_K \rightarrow 0$ while keeping the product $V_0 = J_K S_{\text{imp}}$ constant. In this limit, one finds $w \rightarrow 0$, i.e., the a boson decouples from the $b(\mathbf{r})$ bosons. Then the only effect of the impurity is to act as a static local field on the bulk degrees of freedom.

Noting that the effective Hamiltonian (18) conserves the total magnon number, we use an *Ansatz* for a general single-particle state,

$$|\Psi\rangle = \left(\int d^2r \psi(\mathbf{r}) b^\dagger(\mathbf{r}) + \phi_a a^\dagger \right) |0\rangle, \quad (20)$$

where $\psi(\mathbf{r})$ and ϕ_a are wave functions and $|0\rangle$ is the vacuum state, identified with the ground state of the unperturbed Hamiltonian (for $J_K = 0$). The Schrödinger equation, $H_{\text{eff}}|\Psi\rangle = E|\Psi\rangle$, where the energy E is measured relative to ω_g , yields the coupled equations

$$\begin{aligned} -\frac{1}{2m} \nabla^2 \psi(\mathbf{r}) - V_0 \delta(\mathbf{r}) \psi(\mathbf{r}) + w \phi_a \delta(\mathbf{r}) &= E \psi(\mathbf{r}), \\ \varepsilon_a \phi_a + w \psi(0) &= E \phi_a. \end{aligned} \quad (21)$$

From Eq. (21), we observe that a bound state solution with $E = E_b < 0$ satisfies the relation

$$\phi_a = -\frac{w \psi(0)}{\varepsilon_a + |E_b|}. \quad (22)$$

Substituting Eq. (22) into the first equation in Eq. (21), we obtain the Schrödinger equation for a δ -function potential,

$$-\frac{1}{2m} \nabla^2 \psi(\mathbf{r}) - V_{\text{eff}}(E_b) \delta(\mathbf{r}) \psi(\mathbf{r}) = E_b \psi(\mathbf{r}), \quad (23)$$

with a renormalized coupling that depends on the energy itself,

$$V_{\text{eff}}(E_b) = V_0 + \frac{w^2}{\varepsilon_a + |E_b|}. \quad (24)$$

For a *classical* magnetic impurity, $w \rightarrow 0$ implies that $V_{\text{eff}} = V_0$ is constant. Hence Eq. (23) can be solved after imposing a large-momentum cutoff Λ [59]. The resulting bound state energy is exponentially small at weak coupling but depends on V_0 and m in a nonperturbative manner,

$$E_b \simeq -\frac{\Lambda^2}{2m} e^{-2\pi/(mV_0)}. \quad (25)$$

For a *quantum impurity*, on the other hand, we obtain a qualitatively different scaling of the bound state energy. In this case, $V_{\text{eff}}(E_b)$ becomes large if ε_a is negative and $\varepsilon_a \approx E_b$. In particular, for the Kitaev-Heisenberg model with $g = 1$, we have $\omega_g = h$ and then $\varepsilon_a = -J_K S < 0$ for any $J_K > 0$. In general, the binding energy is given by the solution of the equation

$$\frac{2m|E_b|}{\Lambda^2} = \exp \left[-\frac{2\pi}{mV_{\text{eff}}(E_b)} \right], \quad (26)$$

In the regime $|V_{\text{eff}}(E_b)| \gg 1$, we can approximate

$$\frac{2m|E_b|}{\Lambda^2} \approx 1 - \frac{2\pi}{mV_0 + \frac{mw^2}{\varepsilon_a + |E_b|}}, \quad (27)$$

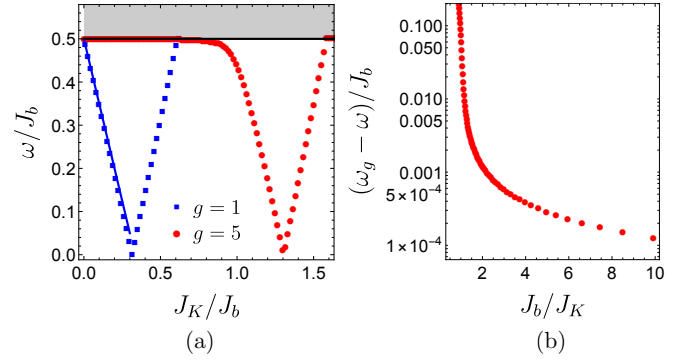


Figure 5. Magnon spectrum ω for the Kitaev-Heisenberg model with an adatom quantum magnetic impurity vs impurity coupling J_K (both ω and J_K are in units of the bulk exchange coupling $J_b > 0$). We set $S = 3/2$, $S_{\text{imp}} = 1/2$, $h/J_b = 0.5$, and $K/J_b = -0.2$, where the field is along the $\hat{\mathbf{c}}$ direction. (a) The symbols represent the bound state energy calculated by LSW theory for $g = 1$ (blue squares) and $g = 5$ (red dots). The solid line for $g = 1$ gives the analytical prediction (28). The shaded region represents the magnon continuum $\omega > \omega_g = h$. (b) Binding energy for $g = 5$ in the weak-coupling regime, plotted on a logarithmic scale vs J_b/J_K .

which is a quadratic equation in $|E_b|$. The low-energy solution is

$$E_b = \varepsilon_a + \mathcal{O}(w^2) = gh - \omega_g - J_K S + \mathcal{O}(J_K^2). \quad (28)$$

For $g = 1$, the binding energy vanishes for $J_K \rightarrow 0$ and scales linearly with J_K at weak coupling. The linear dependence predicted by Eq. (28), without any free fitting parameter, is in excellent agreement with our numerical results for the lattice model, see Fig. 5(a). For $g > 1$, the binding energy is exponentially small at weak coupling, see Fig. 5(b), but it crosses over to the linear dependence as one increases J_K . The condition $w^2/\varepsilon_a \sim V_0$, see Eq. (24), gives the estimate $J_K \sim \frac{(g-1)h}{2S}$ for the crossover scale. In the strong-coupling regime, i.e., above the spin transition, the bound state eventually merges with the continuum and disappears for sufficiently large J_K .

III. On the STS conductance

In this section, we briefly describe how one derives Eq. (M3) for the STS conductance. In order to describe electrical transport through a 2D magnet, one has to start from a model that retains the charge degrees of freedom, e.g., the Hubbard-Kanamori model. By a Schrieffer-Wolff transformation to the low-energy spin sector, one then obtains the Hamiltonian (M1) in terms of spin operators \mathbf{S}_j . We now include tunneling processes with amplitude $t_A(\mathbf{r} - \mathbf{R}_j)$ connecting a normal-conducting scanning probe tip at position \mathbf{r} , described

by noninteracting fermion operators $c_{A,\tau}(\mathbf{r})$ for spin projection $\tau \in \{\uparrow, \downarrow\}$, to lattice site \mathbf{R}_j of the 2D layer. Here we assume that t_A is independent of the momentum and the spin of the tunneling electrons. Similarly, we include tunneling processes with constant amplitude t_B connecting the respective site in the 2D layer to a 2D substrate described by noninteracting fermion operators $c_{B,\tau}(\mathbf{R}_j)$. Below, Pauli matrices $\boldsymbol{\tau} = (\tau_x, \tau_y, \tau_z)$ and the identity τ_0 act in conduction electron spin space. Applying a Schrieffer-Wolff transformation in the presence of these tunneling terms now yields an effective cotunneling Hamiltonian connecting the tip and the substrate via the 2D magnetic layer, see [37, 38, 60–62] for details,

$$H_{\text{cot}} = \sum_j \frac{t_A^*(\mathbf{r} - \mathbf{R}_j)t_B}{U} c_A^\dagger(\mathbf{r})(\eta_0 \tau_0 \mathbb{1}_j + \eta_1 \boldsymbol{\tau} \cdot \mathbf{S}_j) c_B(\mathbf{R}_j) + \text{H.c.}, \quad (29)$$

where the sum runs over all lattice sites of the 2D magnet in Eq. (M1), including the impurity site. Here, U is a Coulomb interaction energy scale of the 2D layer, and $c_{A/B}^\dagger = (c_{A/B,\uparrow}^\dagger, c_{A/B,\downarrow}^\dagger)$. The numbers η_0 and η_1 depend, in particular, on the ratio of the Hund's rule coupling J_H and the parameter U , and are of order unity [38]. (In general, they are different for bulk and impurity sites.) We note in passing that in general there is also a spin-rotation-symmetry breaking contribution [38] which we have neglected in Eq. (29). We assume an exponential distance dependence of the tunneling matrix elements, $t_A(\mathbf{r} - \mathbf{R}_j) \propto e^{-|\mathbf{r} - \mathbf{R}_j|/l_0}$, where the length scale l_0 sets the resolution of the scanning probe tip. We also assume a constant and spin-independent (non-polarized) density of states in the relevant energy range for both the tip (d_A) and the substrate (d_B).

A computation of the current $I(V)$ from tip to substrate, and thus of the differential conductance $G(V) = dI/dV$, can now be performed by perturbation theory in H_{cot} . To that end, we proceed along standard steps, see, e.g., Ref. [38]. Within Fermi's golden rule, the squared matrix elements of $\eta_0 \tau_0 \mathbb{1}_j + \eta_1 \boldsymbol{\tau} \cdot \mathbf{S}_j$ appear. The term $G \propto \eta_0^2$ is associated with elastic tunneling processes and gives rise to a background conductance which is independent of voltage and tip position. The term $G \propto \eta_0 \eta_1$ is also independent of voltage but generally depends on the tip position as it involves the spin expectation values $\langle S_j^\alpha \rangle$. However, it vanishes under the above assumption of a non-polarized tip and substrate. Finally, the term $G \propto \eta_1^2$ depends on voltage in a nontrivial manner since it probes the dynamical spin correlations of the 2D magnet. This term is shown in Eq. (M3). Accounting for the exponential distance dependence of t_A through the form factors $F_{j,k}$ in Eq. (M3), all other microscopic factors in Eq. (29) appear only via the overall scale G_0 for the cotunneling conductance, and through cotunneling amplitudes t_j . For the latter, we distinguish between bulk sites (with $t_{j \neq 0} = t_{\text{bulk}}$) and the impurity

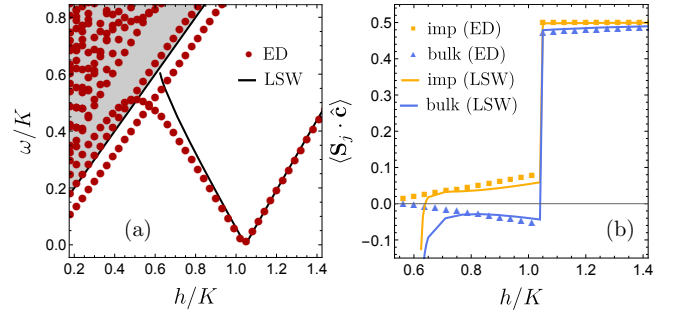


Figure 6. ED and LSW results for a magnetic quantum impurity in the adatom configuration for the ferromagnetic Kitaev model ($K > 0$, $J_b = 0$) with $S = S_{\text{imp}} = 1/2$, $J_K/K = 1.5$, $g = 1.5$, and $\mathbf{h} = h\hat{\mathbf{c}}$. (a) Excitation spectrum vs magnetic field. ED (LSW) results correspond to red dots (black lines). ED results were obtained for a system of 2×2 unit cells with periodic boundary conditions. (b) Spin projections $\langle \mathbf{S}_{0,1} \cdot \hat{\mathbf{c}} \rangle$ vs h/J_b . Yellow squares (lines) correspond to ED (LSW) results for the impurity spin. Results for the coupled bulk spin are shown as blue triangles (ED) and blue lines (LSW), respectively.

site (with $t_{j=0} = t_{\text{imp}}$). The ratio $t_{\text{imp}}/t_{\text{bulk}}$ may vary substantially depending on the impurity type (adatom vs substitutional). In Fig. 3 of the main text, we considered $t_{\text{imp}} > t_{\text{bulk}}$, assuming a stronger overlap of the tip wavefunction with Co adatoms than with Cr^{3+} ions in the honeycomb layer. After the above steps, and taking the zero-temperature limit for simplicity, one arrives at Eq. (M3). The conductance is thereby expressed in terms of dynamical spin correlations of the 2D magnet in the absence of tip and substrate, see Sec. IC. These correlations exhibit a peak at the bound state energy which translates to a step in the conductance. As discussed in the main text, one can thereby track the energy of the bound state as a function of the external magnetic field by measuring $G(V)$ or dG/dV . Moreover, $G(V = 0)$ can directly monitor atomic-scale spin-flip transitions.

IV. Kitaev honeycomb model

We here show results for the ferromagnetic 2D Kitaev honeycomb model with $J_b = 0$ and $K > 0$ [27] in the partially polarized phase, which may serve as idealized model for $\alpha\text{-RuCl}_3$ in a strong magnetic field. For the bulk spins (Ru^{3+}), we effectively have $S = 1/2$. Using Co atoms as examples for the adatom magnetic impurities [22], we have $S_{\text{imp}} = 1/2$ with $g \approx 1.5$. In contrast to Fig. 2(b) of the main text, we now find that the discontinuity in the local magnetization at the transition ($h/K \approx 1.05$) is larger for the bulk than for the impurity spin. In fact, the magnetization of the bulk spin becomes slightly negative for magnetic fields just below the transition. While the spin flip of the bulk spin is expected to occur for the large- g limit, we here observe that it

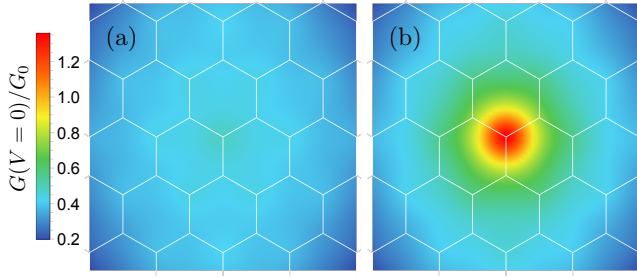


Figure 7. Spatial profile of the zero-bias STS conductance near an adatom magnetic impurity for the ferromagnetic Kitaev model, with the same parameters as in Fig. 6. Results obtained from LSW theory for two field values: (a) $h = 0.854K$ (below the transition), (b) $h = 1.33K$ (above the transition).

can happen already for moderate values of $g > 1$. Despite of the small system size used in the ED calculations, LSW and ED results agree rather well for large magnetic fields. However, Fig. 6 shows that they significantly deviate for $h/K < 0.7$, i.e., once the bound state approaches the continuum. However, since the main emphasis of our work is on spin-flip transitions associated with zero-

energy bound states, we do not study this regime here in detail.

In Fig. 7, we show the spatial profile of the STS zero-bias conductance for the Kitaev model near the adatom impurity studied in Fig. 6. Similar to our results for the Kitaev-Heisenberg model in Fig. 3 of the main text, the zero-bias conductance is significantly enhanced in the vicinity of the impurity for magnetic fields above the transition. In the present case, however, both the impurity and the coupled bulk spin show positive magnetization. In fact, below the critical field, the conductance has a local maximum when the tip is right above the impurity, in contrast to the local minimum observed in Fig. 3(c) of the main text. This difference can be rationalized by noticing that the parameter choice $t_{\text{imp}} > t_{\text{bulk}}$ used in Fig. 7 favors contributions due to cotunneling via the impurity site. The corresponding impurity spin still has a small positive magnetization even below the transition, see Fig. 6(b), in contrast to the negative magnetization observed below the transition in Fig. 2(b) of the main text.